Advanced Materials

ADVANCED MATERIALS
www.advmat.de

RESEARCH ARTICLE

A Non-Equilibrium Flame Aerosol Process to Create High-Entropy MOFs

Shuo Liu[1,2] | Jiashun Liang[1] | Mohd Ashhar Khan[1] | Shaon Das[3] | Jialu Li[4] | Chao Zheng[1] | Sanjit Ghose[5] | Dominik Wierzbicki[5,6] | Qike Jiang[7] | Kaiwen Chen[1] | Christina T. Scalzo[8] | Zhengxi Xuan[1,9] | Sai Varun Karepakula[1] | Yaoli Zhao[1] | Kun Wang[10] | Jinghua Guo[4] | Baishakhi Mazumder[3] | Wei Chen[3] | Kaihang Shi[1] | Gang Wu[1] | Jeffrey J. Urban[2] | Mark T. Swihart[1,9] | Chaochao Dun[2]

[1]Department of Chemical and Biological Engineering, University At Buffalo, The State University of New York, Buffalo, New York, USA | [2]The Molecular Foundry, Lawrence Berkeley National Laboratory, Berkeley, California, USA | [3]Department of Materials Design and Innovation, University At Buffalo, The State University of New York, Buffalo, New York, USA | [4]Advanced Light Source, Lawrence Berkeley National Laboratory, Berkeley, California, USA | [5]National Synchrotron Light Source II, Brookhaven National Laboratory, Upton, New York, USA | [6]Faculty of Energy and Fuels, AGH University of Science and Technology, Cracow, Poland | [7]Instrumentation and Service Center For Physical Sciences, Westlake University, Hangzhou, Zhejiang, China | [8]Magnetic Resonance Center, University At Buffalo, The State University of New York, Buffalo, New York, USA | [9]RENEW Institute, University At Buffalo, The State University of New York, Buffalo, New York, USA | [10]Kazuo Inamori School of Engineering, Alfred University, New York, USA

Correspondence: Jeffrey J. Urban (jjurban@lbl.gov) | Mark T. Swihart (swihart@buffalo.edu) | Chaochao Dun (cdun@lbl.gov)

Received: 8 February 2026 | **Revised:** 11 June 2026 | **Accepted:** 29 June 2026

Keywords: flame spray pyrolysis | high-entropy materials | MOFs | non-equilibrium synthesis

ABSTRACT

High-entropy alloys and ceramics have demonstrated promising applications in the past decade. Ultrafast heating and cooling can kinetically trap immiscible elements into solid solutions, expanding the compositional space and optimizing the properties of high-entropy materials. However, the extreme temperatures required by these non-equilibrium methods are incompatible with metal–organic frameworks (MOFs). This work presents a flame aerosol strategy for synthesizing compositionally complex, entropically stabilized MOFs, enabling new combinations of properties previously inaccessible in this class of materials. Using the HKUST structure as a prototype, this methodology is extended to a wide array of both crystalline and amorphous MOFs, and then to a 10-element MOF that incorporates transition metals, rare-earth metals, alkaline-earth metals, p-block metals, and noble metals. This strategy can be further applied to inorganic coordination polymers. This study reveals that kinetics and entropy collectively drive structural short-range periodicity and configurational disorder in the framework, which in turn influence crystallinity, pore architecture, defect density, homogeneity, and electrochemical properties. This work expands the compositional design space for MOFs and offers new opportunities for their fundamental study and practical application.

1 | Introduction

Numerous reports over the past decade have demonstrated the potential of high-entropy alloys, high-entropy oxides, and related compositionally complex materials to achieve combinations of properties that are otherwise inaccessible [1]. Such high-entropy materials incorporate five or more metallic elements at comparable compositions (5 to 35 at.%) within a single-phase structure. Their unique performance arises from the associated configurational entropy, which stabilizes phases that might otherwise segregate and induces distinctive effects such as sluggish diffusion, lattice distortion, and cocktail effects [2]. These emergent phenomena have enabled superior performance across a wide range of applications compared to their unary or

binary counterparts [3]. In contrast, metal–organic frameworks (MOFs) typically incorporate only one or two types of metal centers, due in part to the kinetic and thermodynamic limitations of conventional synthesis methods, especially approaches using solution-phase self-assembly under mild conditions that dominate the field [4]. These methods favor highly crystalline structures but are poorly suited to incorporate multiple metals with disparate coordination preferences, hydrolysis behaviors, and redox properties. Although multivariate MOFs, that is, those containing multiple metal or linker types, have emerged as a subfield, the multiple metals incorporated share the same preferred coordination geometry rather than exhibiting substantial differences in valence or chemical behavior [5]. Similarly, a few recent studies have introduced the "high-entropy" concept into MOF materials [6–8], in which the incorporated metals usually exhibit an elementally disordered distribution within the framework. These high-entropy MOFs demonstrate promising performance enhancements in applications such as sodium storage [9], photocatalytic hydrogen evolution [10], and CO_2 fixation [11].

However, synthesis of high-entropy MOFs (and multivariate MOFs) has relied on conventional solvothermal methods, mechanochemical synthesis, or electrodeposition synthesis, which limits the metals incorporated to those with closely matched ionic radii and chemical behavior [12–14]. Incorporating elements with significantly different chemical behavior, such as noble metals, into a MOF may greatly enhance its performance. A notable example is MOF-based single-atom catalysts [15]. The integration of a noble metal into the MOF lattice or bound to a secondary metallo-ligand introduces atomically dispersed active sites, significantly enhancing catalytic performance. However, introduction of such heteroatoms typically requires specific coordination environments, ionic valence states, or post-synthetic modifications [16], which greatly limit the concentration and variety of guest metals. Mixing of multiple heteroatoms of varied types into a single-phase MOF in flexible ratios has not previously been achieved.

In alloy and ceramic solid solution materials, thermodynamically unfavorable mixing of elements of different chemical nature has been addressed through rapid reaction kinetics. Several extreme, non-equilibrium synthesis methods, such as extreme-temperature plasma [17], laser scanning ablation [18], and flash Joule heating [19], have been developed to combine thermodynamically immiscible elements. These methods enable ultrafast material formation within milliseconds or even nanoseconds, producing metastable (kinetically stabilized) materials. In such cases, even when the formation of a homogeneous solid solution is thermodynamically unfavorable, separation of these phases via diffusion is too slow compared to the rapid heating and cooling timescales, effectively trapping the immiscible metals in a single metastable phase [20]. Meanwhile, the increase in configurational entropy associated with multiple components further promotes the uniform distribution of elements [21]. For example, the synergy of rapid reaction kinetics and configurational entropy enabled the formation of high-entropy alloy nanoparticles composed of 15 immiscible elements [22]. Unfortunately, these extreme synthesis techniques are not suitable for MOFs, as the ultrahigh reaction temperatures would rapidly degrade organic linkers.

Therefore, a versatile methodology for incorporating a range of diverse and dissimilar metals in a homogeneous high-entropy MOF matrix is both a major challenge and a substantial opportunity. In the absence of such a general methodology, the roles of kinetics and configurational entropy on compositionally complex MOF structures remain unclear. Here, we report a general method for creating compositionally complex (high-entropy) MOFs, to address these challenges, based on a unique flame aerosol process [23–25]. We have applied this approach to a broad range of crystalline and amorphous MOFs, as well as metal–inorganic frameworks. Furthermore, this non-equilibrium flame aerosol process enables the integration of multiple elements, including typically immiscible species, into a single-phase high-entropy MOF lattice. Based on the "cocktail effect" of high-entropy materials, the synergistic interactions among elements in multinary solid solutions often lead to properties that surpass those of individual constituents and sometimes can even result in unprecedented functionalities [26, 27]. Thus, this approach greatly expands the accessible compositional space of high-entropy MOFs and allows for systematic optimization of their performance through flexible elemental selection across various functional applications. Meanwhile, we show that rapid reaction kinetics and configurational entropy induce substantial disorder in the materials' periodic arrangement and elemental distribution, impacting crystallinity, pore structure, defect density, and electrochemical performance.

2 | Results and Discussion

2.1 | Aerosol Synthesis of High-Entropy MOFs

We produced high-entropy MOFs using a continuous, one-step flame aerosol process, as described in detail in the Methods section (Figures 1a, S1, Tables S1–S2). The liquid precursor (comprising five or more metal salts, one organic linker, and a mixed solvent) was continuously injected into the reactor, while the MOF product was simultaneously collected downstream. The high-entropy MOF was formed via rapid droplet-to-particle conversion. Upon injection into the reactor, the precursor solution was shear-atomized into droplets with diameters of a few micrometers by a high-velocity hot gas stream [28]. Rapid solvent evaporation increased the concentration of reactants within the droplets, facilitating the coordination between metal ions and the organic linker. Evaporation occurred at the droplet surface, generating a higher concentration of reactants at the surface during the droplet-to-particle transition. Thus, the assembly of metal ions and the ligand initiated at the droplet surface, followed by inward growth, often leading to the formation of a hollow nanoshell morphology [29].

Despite the high-temperature environment, the ultrafast droplet-to-particle conversion (within a few milliseconds) [30] and immediate quenching by a large nitrogen flow suppress thermal degradation of the organic linkers, enabling successful MOF formation. Unlike traditional solvothermal synthesis, which occurs near thermodynamic equilibrium and over an extended time, flame–aerosol synthesis is a far-from-equilibrium process governed by rates of reaction and diffusion. The brief residence time of a few milliseconds and the rapid quenching prevent side reactions such as linker decomposition, and phase separation.

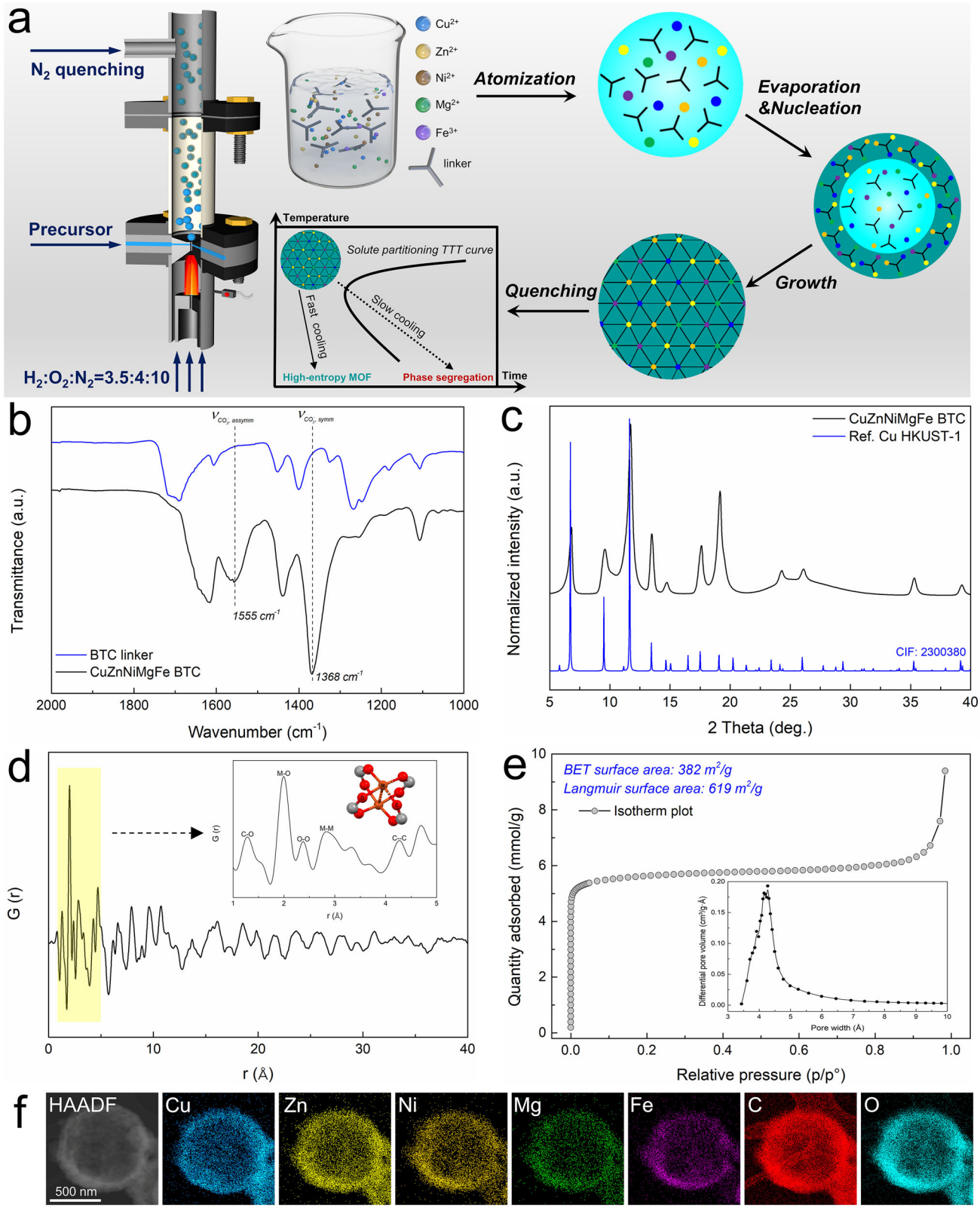

FIGURE 1 | High-entropy MOF formed through rapid reaction kinetics. (a) Schematic of high-entropy MOF produced in non-equilibrium flame aerosol process; (b) FTIR spectra, (c) XRD pattern, (d) PDF from X-ray scattering, (e) N_2 adsorption isotherm plot and Horvath–Kawazoe differential pore volume plot, and (f) HAADF-STEM EDS elemental maps of a representative CuZnNiMgFe BTC high-entropy MOF.

This enables the preservation of the coordination network and the retention of MOF structural features even under high-temperature (~400°C) conditions. Moreover, this process maintains the random, homogeneous, and disordered distribution of metal ions from the precursor solution in the final MOF product. The increase in configurational entropy in the multi-element MOF further promotes the uniform distribution of elements [31]. In the multi-element MOF, different metals occupy the same metal node positions, and the connected oxygen anions create an almost indistinguishable nearest-neighbor environment, reducing the energy differences between different elements in the same environment, collectively enhancing energetic degeneracy [32].

The CuZnNiMgFe BTC (BTC = 1,3,5-benzenetricarboxylate) high-entropy MOF produced as described above serves as a prototypical example, which we characterized in detail. The formation of coordination bonds between metal ions and BTC linkers was confirmed by Fourier transform infrared (FTIR) spectroscopy (Figure 1b). New absorbance peaks at 1368 and 1555 cm^{-1} were observed, corresponding to the symmetric and asymmetric stretching vibrations of the coordinated carboxyl groups [33]. The BTC linker was detected by hydrogen nuclear magnetic resonance (1H NMR) spectroscopy (Figure S2), and all the metal ions were also detected in the X-ray photoelectron spectrum (XPS) (Figure S3). Compared with the single-element Cu BTC MOF, the Cu^{2+} XPS peaks of the high-entropy MOF exhibit obvious deviations, reflecting the modulation of the local electronic environment by neighboring heterometallic centers, consistent with the well-mixed configuration of multiple metals within the framework rather than isolated Cu sites (Figure S4) [14, 34]. The X-ray diffraction (XRD) pattern matched that of typical HKUST-1 structured $Cu_3(BTC)_2$ MOF, without any additional peaks or evidence of secondary phases (Figure 1c). Moreover, the detailed structure was probed by X-ray total scattering, from which we obtained the pair distribution function (PDF) (Figures 1d, S5). The short-range (1–6 Å) PDF pattern matched that of conventional Cu HKUST-1 MOF [35], for which the interatomic distances corresponded to the $M_2(CO_2)_4$ secondary building unit. However, the PDF signal at longer distance was weak, indicating the reduced periodicity of the high-entropy MOF. N_2 sorption analysis yielded a type I isotherm, indicating the microporous nature of the high-entropy MOF. Pore volume was estimated by the Horvath–Kawazoe method, which gave a pore size distribution from 3 to 6 Å (Figure 1e). The BET surface area was lower than that of conventional Cu HKUST-1. Most importantly, high-angle annular dark-field scanning transmission electron microscopy (HAADF-STEM) with elemental mapping by EDS (Figure 1f) confirmed the uniform elemental distribution. To further investigate the microscopic dispersion of the metals, aberration corrected scanning transmission electron microscopy (AC-STEM) was employed and the high-resolution EDS maps demonstrated the homogeneous distribution of all the constituent elements at the atomic scale (Figure S6). Most of the particles exhibited a hollow nanoshell morphology. The nanoshells were polydisperse in size with a geometric mean diameter of 452 nm (Figure S7). DSC-TGA analysis confirmed stoichiometry close to that of typical Cu HKUST-1 (Figure S8), [33] and the FTIR of CuZnNiMgFe BTC high-entropy MOF at a higher synthesis temperature of 500°C matched that of the MOF synthesized at 400 °C (Figure S9), demonstrating excellent thermal stability and showing that the ultra-fast flame aerosol process did not destroy the MOF structure, even when the reaction temperature exceeds the MOF thermal decomposition temperature. Together, these material characterization results conclusively demonstrate the successful synthesis of a single-phase, homogeneous high-entropy MOF.

2.2 | Entropy-Engineered MOF Structural Evolution

To explore the role of entropy in the MOF structure, we conducted density functional theory (DFT) calculations to simulate HKUST structures containing 1 to 5 metal elements, including Cu BTC, binary CuZn BTC, ternary CuZnNi BTC, quaternary CuZnNiMg BTC, and high-entropy CuZnNiMgFe BTC (Figure 2a). In the multi-metal MOFs, Cu atoms in Cu BTC were randomly replaced with other metal atoms (Table S3) to generate the initial HKUST structures, which were then optimized. DFT-optimized structures retained the overall HKUST crystal structure, but lattice distortion and appreciable atomic displacement were observed upon introduction of additional metal elements. Such structural distortion is reflected by the reduced intensities of primary peaks at $2\theta = 6.7°$, 9.5°, and 11.6° in the corresponding simulated XRD patterns (Figure 2b). However, we note that DFT based geometry optimization cannot fully capture the influence of kinetic factors or the stabilizing role of configurational entropy under non-equilibrium synthesis conditions, such as those present in flame aerosol processing.

To gain deeper understanding of the role of configurational entropy in the structure of multi-element MOFs under non-equilibrium reaction conditions, we experimentally synthesized unary to quaternary MOFs using the same elements, as well as the high-entropy MOF shown in Figure 1. Inductively coupled plasma (ICP) analysis showed their elemental composition and the calculated configurational entropy (here, we adopt the concept from alloy and ceramic solid solution materials, $\Delta S = -R\sum_{i=1}^{n} x_i \ln x_i$, calculating based on the number and ratios of metal elements in the multi-element MOF assuming ideal mixing) (Table S4). The configurational entropy of CuZnNiMgFe BTC MOF is 1.55R, exceeding the 1.5R threshold commonly defined for high-entropy materials [31]. Overall, the rapid aerosol process, unlike equilibrium solvothermal methods, does not provide enough reaction time for nucleation and growth of MOF single crystals. Rapid solvent evaporation leads to multiple nucleation sites within each droplet. As a result, the BTC MOFs produced via this method exhibited a polycrystalline, hollow microsphere morphology, homogeneous elemental distribution with numerous tens-of-nanometer MOF nanocrystals packed into a compact shell (Figures 2c, S10–S12). Experimental XRD patterns and the normalized results exhibited primary peaks at $2\theta = 6.7°$, 9.5°, and 11.6°, which align with the positions in the simulated XRD patterns, demonstrating the successful preparation of single-phase MOFs with the HKUST-1 crystal structure in all cases (Figures 2c and S13). However, unlike the structures predicted by DFT calculations, these kinetically stabilized MOFs presented significant differences in long-range periodicity. The CuZnNiMgFe BTC high-entropy MOF showed obviously lower crystallinity and smaller effective grain size than others, as determined by the Scherrer equation applied to the peak at $2\theta \sim 11.6°$ (Tables S5–S9). At short range, however, these

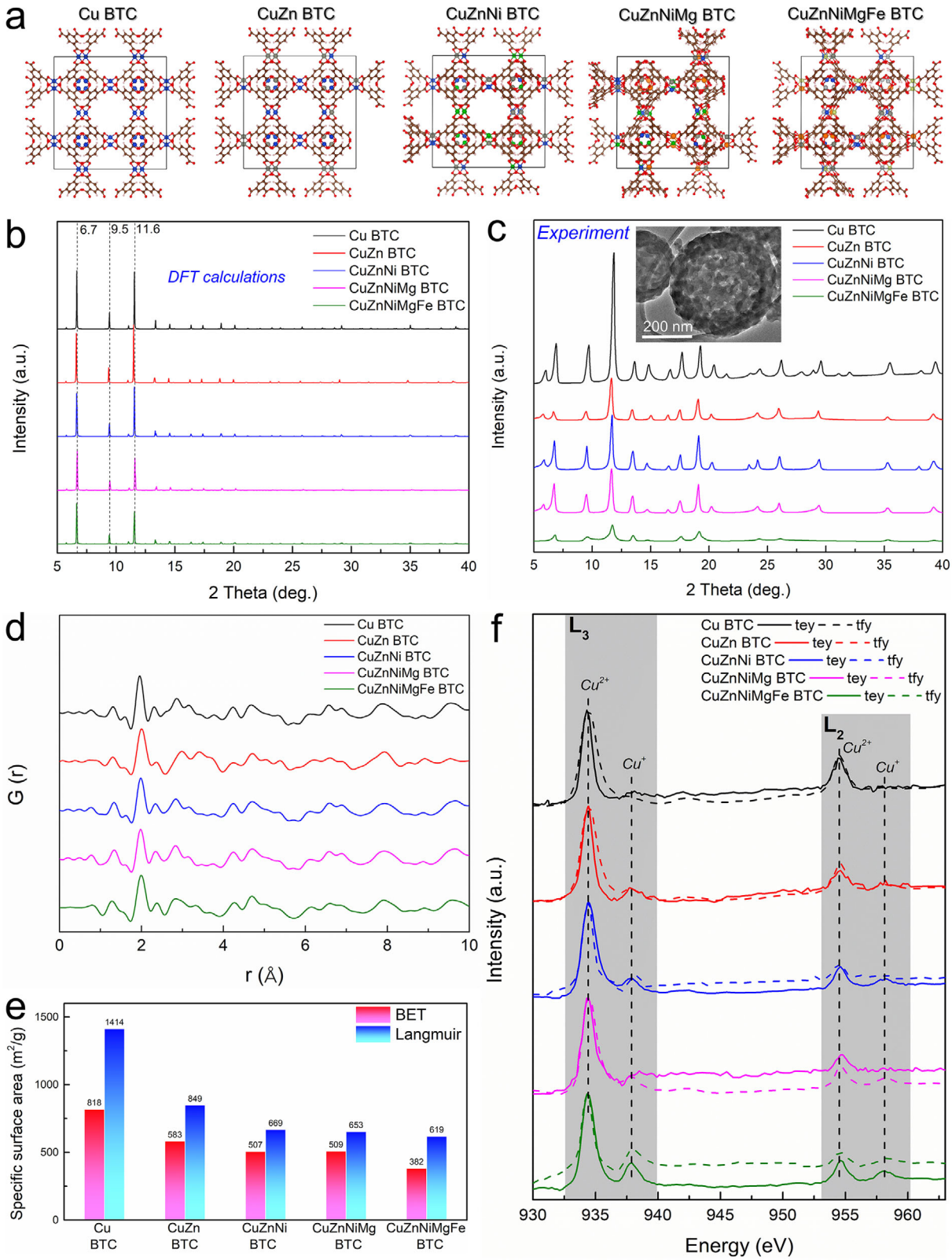

FIGURE 2 | Modulating MOF architectures through strategic manipulation of configurational entropy. (a) DFT-optimized MOF structures and (b) corresponding simulated XRD patterns; Experimental (c) XRD patterns and representative TEM image, (d) PDF patterns, (e) specific surface areas, and (f) Cu L-edge sXAS spectra of unary to quinary BTC MOFs.

kinetically stabilized BTC MOFs presented the same level of ordering. Their PDF patterns all correspond to the same $M_2(CO_2)_4$ cluster (Figures 2d, S5, and S14–S17). Therefore, in kinetically stabilized multi-element MOFs, configurational entropy influences long-range periodicity without significantly perturbing short-range order. Meanwhile, the simulated PDFs derived from DFT show a first M—O peak at ~2.0 Å, consistent with the experimental PDF results, confirming equivalent and averaged metal–oxygen coordination in the high-entropy MOFs (Figure S18).

Variations in MOF crystallinity affected MOF porosity and the concentration of structural defects. The reduction in specific surface area with increasing configurational entropy (Figures 2e and S19) is primarily attributed to the higher defect concentration in high-entropy MOFs. The increased structural disorder and defects partially collapse the internal microporous framework, thereby decreasing the specific surface area. Meanwhile, randomly incorporating elements with different valences and atomic radii into the same nominal metal node sites altered the coordination environment and introduced point defects. The local chemical state of Cu in MOFs was detected by soft-line X-ray absorption spectra (sXAS) in both the surface-sensitive total electron yield (TEY, < 5 nm) mode and the in-depth total fluorescence yield (TFY, >100 nm) mode (Figure 2f). The L_3 edge and L_2 edge correspond to Cu $2p^{3/2} \rightarrow 3d^{3/2}3d^{5/2}$ and $2p^{1/2} \rightarrow 3d^{3/2}$, respectively. The spectra featured main absorption edges at ~934 eV (L_3) and ~954 eV (L_2) of Cu^{2+} ions, as well as pre-edges at ~938 eV (L_3) and ~958 eV (L_2) of Cu^{+} ions [36]. The ratio of Cu^{+}/Cu^{2+} from sXAS spectra can reflect the concentration of defect sites in HKUST-1 MOF. Gaussian fitting results for the Cu L-edge sXAS peaks in the TEY mode are shown in Table S12 and in the TFY mode are shown in Table S13. The Cu^{+}/Cu^{2+} ratio in the CuZnNiMgFe high-entropy BTC MOF was significantly higher than others for both TEY and TFY modes, indicating a higher defect density both on the surface and throughout the bulk of the MOF.

Therefore, the high-entropy MOF exhibits a structure significantly different from unary and other multi-element MOFs, likely due to the incorporation of Fe ions. Unlike the other four elements, which predominantly exhibit a +2 oxidation state, Fe commonly adopts both +2 and +3 states. These variations in nominal oxidation state during coordination disrupt the long-range periodicity and generate additional defects. To verify this hypothesis, we replaced Fe with another multivalent element Co and synthesized another high-entropy MOF CuZnNiMgCo BTC (Tables S3 and S10). The coordination between the metal ions and the BTC linker (Figure S20), along with the homogeneous distribution of each element (Figure S21), confirmed the successful synthesis of the CuZnNiMgCo high-entropy MOF. In addition, to further investigate the impact of kinetics on MOF crystallization, we synthesized a conventional Cu HKUST-1 MOF using an equilibrium solvothermal method (Table S11). Similarly, the CuZnNiMgCo BTC MOF also exhibited extremely low crystallinity, even lower than that of CuZnNiMgFe BTC. As a reference sample, Cu HKUST-1 synthesized via a solvothermal method under equilibrium reaction conditions exhibited a large single-crystal morphology, high crystallinity, and high BET surface area (Figures S22 and S23). Figure S24 summarizes the XRD patterns of all BTC MOFs and their calculated crystallite sizes, confirming that rapid non-equilibrium reaction can reduce the long-range order of MOFs. Figures S25 and S26 show that the high-entropy MOF crystallinity can be tuned by the elemental ratio and types. Meanwhile, the four non-Cu single-metal components synthesized by the flame aerosol process did not show a well-crystallized HKUST structure (Figure S27). This proves that the non-equilibrium flame aerosol process can integrate immiscible elements into a single-phase high-entropy MOF and also explains the primary role of Cu in stabilizing the HKUST structure. These findings collectively demonstrate that configurational entropy, in conjunction with fast non-equilibrium synthesis, drives the formation of structurally disordered yet locally ordered high-entropy MOFs with tunable crystallinity, porosity, and defect densities.

2.3 | Extending the Scope to Additional MOFs

To demonstrate the versatility of rapid reaction kinetics in integrating multiple metals into MOFs, we extended this approach to a diverse range of high-entropy MOFs by combining various metal ions and organic linkers (Table 1). These five representative systems span transition metals, lanthanides, and main-group elements, coordinated with chemically distinct organic linkers, highlighting the versatility and universality of high-entropy MOF synthesis under rapid, non-equilibrium conditions. Their chemical composition was confirmed by ICP analysis, and all calculated configurational entropies exceeded 1.5R (Table S14). FTIR spectra showed that new chemical bonds appeared in all as-synthesized high-entropy MOFs, demonstrating the successful coordination between metal ions and organic ligands (Figures S28–32). Meanwhile, the organic linkers were detected by 1H NMR (Figures S33–37), and all the constituent metal ions and chemical states in each high-entropy MOF were also confirmed by XPS spectroscopy (Figures S38–42). TGA analysis showed their good thermal stability at temperatures over 300°C (Figure S43). Most of the high-entropy MOFs were microsphere particles with hollow or solid morphology, and both SEM and TEM elemental maps revealed the homogeneous distribution of all the constituent elements in each high-entropy MOF without any aggregation, demonstrating their high configurational disorder (Figures S44–S53).

The XRD pattern of PrNdTbDyEr PDA high-entropy MOF matched that of conventional lanthanide coordination polymers $Ln_2(PDA)_3$ [37], with a calculated grain size of 23.9 nm based on the XRD peak at $2\theta = 8.3°$ (Figure S54, Table S15). However, as discussed above, the rapid reaction kinetics and the increased configurational entropy in multi-element MOFs significantly reduce the long-range periodicity. This is not only applicable to HKUST MOFs but represents a more general conclusion. The reduction in the degree of order in the other four high-entropy MOFs led to them being effectively amorphous (Figure S55). X-ray total scattering was employed to further investigate the detailed structure of high-entropy MOFs (Figures S56–60). No obvious peaks were observed beyond distances of ~10 Å in their PDF patterns, indicating the absence of long-range periodicity in both the crystalline and amorphous high-entropy MOFs. However, distinct peaks corresponding to atomic pairs were observed within a distance of 5 Å, associated with the basic building blocks of the MOFs, confirming the presence of short-range order.

TABLE 1 | Comparison of MOFs created by the non-equilibrium aerosol process and equilibrium liquid-phase reaction process.

Linker	Metals	Periodicity	Characteristics	Source
PDA 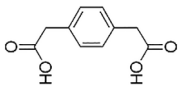	Er	Crystal	The non-equilibrium reaction kinetics and configuration entropy reduces grain size (crystallinity) for lanthanide MOFs	Ref. [35]
	PrNdTbDyEr	Poly-crystal		This research
PMA 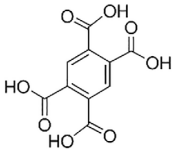	NiFeMn	Crystal	The non-equilibrium reaction kinetics benefit the formation of amorphous MOFs	Ref. [36]
	CuZnNiMgCo	Amorphous		This research
DHTA 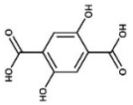	MgCaSrBaMnFeCoNiZnCd	Crystal	The non-equilibrium reaction kinetics play a more important role to lower the periodicity than configurational entropy	Ref. [37]
	CuZnNiMgCo	Amorphous		This research
FMA 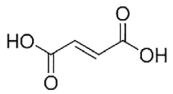	Zr//Fe/Al/Zn	Crystal (different)	Incorporation of 2~4 valence metals with different MOF structures illustrates exceptional framework adaptability across a broad oxidation-state window	Refs. [38, 39, 40]
	ZrHfFeAlZn	Amorphous		This research
BDC-NH_2 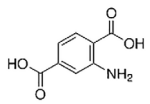	Zr	Crystal → Amorphous	Directly forms the amorphous phase without the need for post-amorphization treatment	Ref. [41]
	ZrHfLaCePr	Amorphous		This research

In summary, compared to single-component, multivariate, and amorphous MOFs synthesized via equilibrium methods [37–43], these MOFs demonstrate the ability of non-equilibrium processes to form polycrystalline and amorphous structures, as well as to integrate metal ions with different oxidation states (Table 1).

2.4 | Designing Disorder in MOFs

The synergistic interaction between different metals in a configurationally disordered MOF can significantly enhance its performance in applications such as catalysis. However, due to the immiscibility of different metals in MOF solid solutions, previously reported multi-element or high-entropy MOFs have employed elements with similar physicochemical properties that form the same MOF structures individually [9–11]. For example, the 10-element MgCaSrBaMnFeCoNiZnCd MOF-74 can be synthesized by near-equilibrium solvothermal reaction because the single-component MOFs of these elements share the same di-valent metal state, $M_3O_3(CO_2)_3$ nodes, and MOF-74 crystal structure [39]. Otherwise, macroscopic phase separation would likely occur. This is commonly observed in MOF-based single-atom catalysts, where noble metals often cannot be fully incorporated into the metal nodes and instead aggregate to form metal nanoparticles on the MOF surface [16].

Thermodynamically, the elemental immiscibility can be overcome by increasing configurational entropy. In the standard expression for Gibbs energy change of mixing, $\Delta G = \Delta H - T\bullet\Delta S$ [2], ΔH is the enthalpic penalty for solid solution formation, typically resulting from differences in crystal structures, valence states, atomic radii, and electronegativities among the components. In contrast, $T\bullet\Delta S$ represents the entropic driving force for solid solution formation. For example, if we consider integrating the UiO-66 phase Zr BDC (solute) into an amorphous multi-element MOF solid solution (solvent), the phase transition enthalpy ($x_{\text{Zr BDC}}\bullet\Delta G^{\text{UiO-66}\rightarrow\text{amorphous}}$) represents an energy barrier that must be overcome. The use of a high-entropy solvent phase helps to lower the overall Gibbs energy ($\Delta G^{\text{amorphous}}{}_{\text{total}}$) for formation of the solid solution by increasing the mixing entropy ($-T\bullet\Delta S_{\text{mix}}$) (Figure S61) [44]. Therefore, the high-entropy MOF as solvent provides an entropic driving force to dissolve the otherwise immiscible phase. Compared to alloy or ceramic solid solution materials, such phase transitions are often difficult to observe in MOFs because their transition temperatures typically exceed their decomposition temperatures. An exception to this is the ZIF family. Crystalline ZIF-4 transitions to an amorphous state upon heating, with the transformation occurring at a glass transition temperature of approximately 300°C [45].

Kinetically, the above thermodynamic rules can be disrupted through ultrafast material formation and quenching processes, enabling higher solubility for non-isostructural components. Our previous research demonstrated this point in metal oxide materials, such as incorporating up to 22 elements into a single-phase fluorite structure [23, 25]. This study demonstrates that the same principle can also be extended to MOFs. In the "droplet-to-particle" MOF formation process occurring on a millisecond timescale, even when forming a single phase is thermodynamically unfavorable, the immiscible elements do not have enough time to diffuse into separate phases. Instead, they are incorporated into a single metastable MOF structure. Subsequent N_2 quenching preserves the structure formed at high temperature, maintaining the high-entropy, high-enthalpy, and disordered metastable state. This process enables the transformation of randomly distributed metal ions in the liquid precursor solution into solid MOF materials, preserving their high configurational disorder, which provides a universal method for preparing high-entropy MOFs with nearly any combination of elements and ratios (Figure 3a).

To demonstrate the above inference, we selected the BDC-NH_2 linker and chose 10 different metals to synthesize a more compositionally-complex high-entropy MOF. These elements were sourced from different regions of the periodic table, including noble metal, transition metal, p-block metal, alkaline earth metal, and rare earth metal elements. These metal ions exhibit varying valences and ionic radii, and as a result, adopt different single-element MOF structures when coordinated with the BDC-NH_2 linker. In ZrHfLaCePrYMgAlNiPt BDC-NH_2 high-entropy MOF, ICP analysis revealed that these elements are present at similar concentrations, with a high configurational entropy of 2.25R (Table S16). Meanwhile, the 10-metal high-entropy MOF exhibited successful coordination between metal ions and the organic linker (Figure S62 and S63), thermal stability (Figure S64), amorphous structure (Figure S65), and short-range order (Figure S66). TEM and SEM elemental maps revealed the homogeneous distribution of all the constituent metals, indicating that all the metals were incorporated into the MOF framework (Figures 3b, S67, and S68). Furthermore, AC-STEM was employed for the 10-metal high-entropy MOF (Figure 3c), showing that isolated atoms were clearly observed as randomly dispersed bright spots, with no detectable aggregated metal nanoparticles or other forms of agglomeration. High-resolution EDS maps demonstrated the homogeneous distribution of all the constituent elements at the atomic scale (Figure S69). This observation aligns with a previous report that utilized entropic stabilization to disperse single-atom active sites within a high-entropy oxide support [46].

The Pt—O bond is very weak and prone to breaking and forming metallic Pt nanoparticles during synthesis [47]. However, no metallic Pt or other separated phases were observed in the XPS and XRD analysis (Figures S63 and S65). To further confirm the dispersion of Pt atoms, hard-line X-ray absorption spectroscopy (hXAS) was performed to determine the coordination environment of Pt in the high-entropy MOF. Pt L_3-edge X-ray absorption near edge structure (XANES) spectra were recorded for the 10-metal high-entropy MOF, as well as PtO_2 and Pt foil as references (Figure 3d). The intense edge feature originated from a $2p^{3/2}\rightarrow 5d$ electron transition. The intensity of the Pt XANES spectra is strongly correlated with oxidation state. The Fourier-transform extended X-ray absorption fine structure (EXAFS) spectra showed the Pt—O bond, which formed by the coordination of Pt ion with BDC-NH_2 linker (Figure 3e). Compared to the PtO_2 reference, the Pt—O bond position exhibited a slight shift due to differences in the local coordination environment and electronic structure of Pt species between the MOF and oxide. No pronounced Pt–Pt coordination shell characteristic of metallic Pt clusters was evident in EXAFS. Similarly, the corresponding wavelet transform (WT) showed a scattering signal centered at 5–7 $Å^{-1}$ in k-space and 1.5–2.0 Å in R-space, closely resembling PtO_2, but distinct from the Pt–Pt coordination peak of Pt foil,

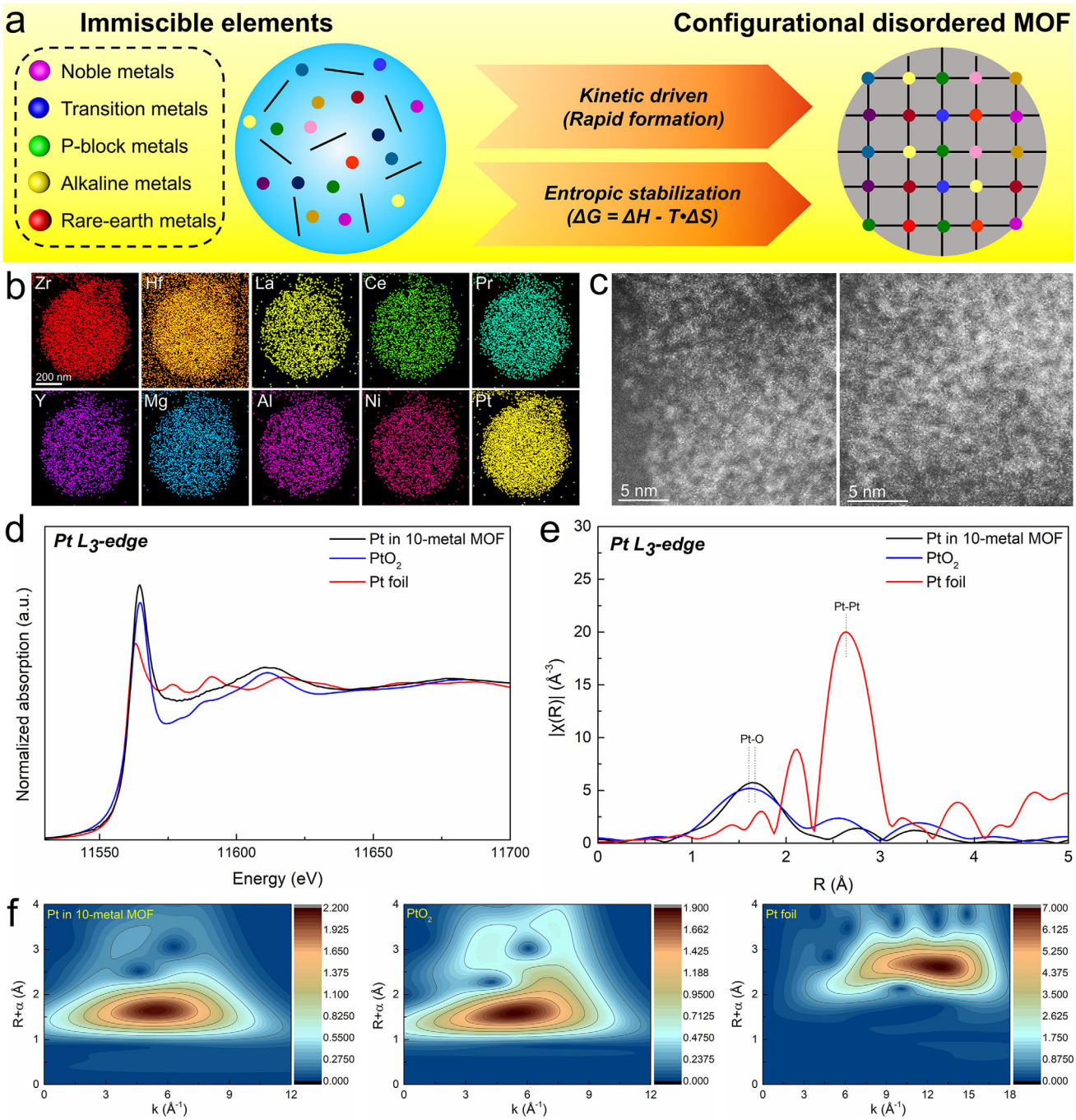

FIGURE 3 | Overcoming the immiscibility of elements through rapid reaction kinetics and maximization of configurational entropy. (a) Schematic of combining immiscible elements in a single MOF phase; (b) HAADF-STEM elemental maps, (c) AC-STEM images of a representative 10-metal ZrHfLaCePrYMgAlNiPt BDC-NH_2 high-entropy MOF; (d) hardX-ray XANES spectra at the Pt L_3-edge, (**e**) k^2-weighted Fourier transform of Pt L_3-edge EXAFS spectra, and (f) the corresponding wavelet transform of Pt in the 10-metal MOF, Pt foil, and PtO_2 references.

which appears around 10 $Å^{-1}$ in k-space and ~2.5 Å in R-space (Figure 3f). This indicates that Pt is coordinated with O atoms from the organic ligands, without formation of metallic Pt clusters, demonstrating the homogeneous dispersion of Pt at the atomic level. Quantitative EXAFS fitting (Table S17) yielded a Pt–O coordination number of 5.8 ± 0.4 with an average bond distance of 2.03 ± 0.01 Å, confirming a well-defined oxygen-coordinated environment around Pt. A weak second-shell Pt–Pt contribution (CN = 1.6 ± 0.5) was detected, which was markedly lower than those of PtO_2 (CN = 8.5) and Pt foil (CN = 12), indicating the absence of PtO_2-like domains or metallic Pt clusters. The slightly elongated Pt—O bond distance relative to PtO_2 suggests a distinct local coordination environment associated with incorporation of Pt into the multimetallic MOF framework. Typically, achieving a loading of single-atom active sites exceeding 2% is challenging [48]. However, here we attained 9.7 mol.% of Pt single atoms without aggregation (Table S16), demonstrating the significant role of rapid reaction kinetics and configurational entropy in

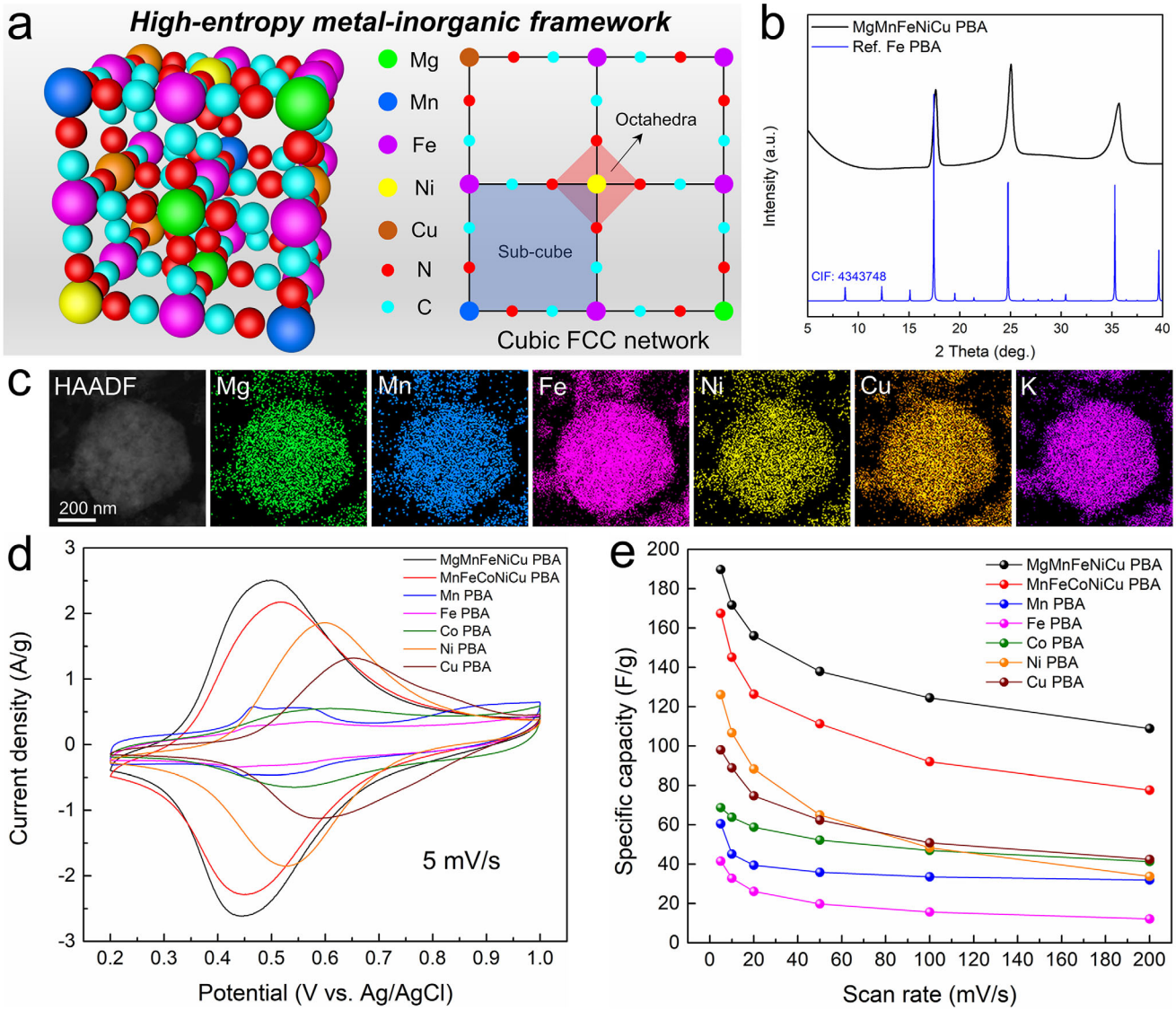

FIGURE 4 | Kinetically and entropically stabilized metal-inorganic framework. (a) Structure of high-entropy PBA; (b) XRD pattern and (c) HAADF-STEM EDS elemental maps of MgMnFeNiCu PBA; (d) CV curves of single-component and high-entropy PBA frameworks at a scan rate of 5 mV/s; (e) Calculated specific capacitances at varied scan rates from 5 to 200 mV/s.

promoting homogeneous elemental dispersion. The atomic-level uniform dispersion of metals such as Zr, Hf, La, Ce, Pr, Y, Mg, Al, Ni, and Pt within the high-entropy MOF aligns closely with the characteristics of recently developed multi-metallic single-atom catalysts [49, 50]. This provides new insights into the design of multi-element MOFs and their potential for application in catalysis. This ability to tailor the elemental composition of MOFs by incorporating dissimilar elements enables flexible, application-oriented design of MOFs for specific reactions. For example, an amorphous high-entropy RuRhPdIrPtFe BDC-NH_2 MOF incorporating five Pt-group metals (PGMs) along with iron (Ru:Rh:Pd:Ir:Pt:Fe = 2:2:2:2:2:90 molar ratio) (Figure S70) was studied for proton exchange membrane water electrolysis (PEMWE) with low PGM loading [51–53]. This MOF showed excellent hydrogen evolution reaction (HER) activity (Figure S71) and 800 h stability in a membrane electrode assembly (MEA) (Figure S72).

2.5 | Atomic 3D Elemental Distribution

Local chemical ordering in high-entropy materials sometimes provides better performance than completely disordered solid solutions [54]. High-resolution TEM can detect local elemental ordering in alloy nanoparticles with a clear crystal lattice [55] but may fail to capture it in MOFs. In contrast, atom probe tomography (APT) provides sub-nanometer spatial resolution and is among the most precise techniques for mapping elements [31, 56]. Here, two representative high-entropy MOFs, crystalline CuZnNiMgFe BTC (Figure 1) and amorphous ZrHfLaCePrYMgAlNiPt BDC-NH_2 (Figure 3), were fabricated into tips by focused ion beam (FIB) milling for APT analysis (Figure S73). For the APT 3D reconstructions, approximately 8 million ions were collected for CuZnNiMgFe BTC, and 6 million ions were collected for ZrHfLaCePrYMgAlNiPt BDC-NH_2. In general, all the detected elements in both MOFs demonstrated a

homogeneous distribution, with no phase separation, elemental segregation, or clustering [57] observed (Supplementary video 1, 2, Figures S74 and S75). This is consistent with the results obtained from EDS mapping and XAS, demonstrating atomic-level homogeneity of the kinetically and entropically stabilized MOFs. Meanwhile, the nearest neighbor distribution (NND) of Ni and Fe in CuZnNiMgFe BTC (Figure S74) and of Zr and Pt in ZrHfLaCePrYMgAlNiPt BDC-NH_2 (Figure S75) showed moderate deviations from a random distribution, confirming the presence of some degree of short-range ordering. This is consistent with the short-range ordering observed in high-entropy alloy [54] and high-entropy ceramic [58] materials. In addition, the configurational short-range ordering discussed here is different from the short-range periodicity mentioned earlier. Here, it refers to the locally inhomogeneous distribution of elements within the MOF solid solution, while the short-range crystalline order refers to the reduction of crystallinity and grain size in the polycrystalline/amorphous MOF structures.

2.6 | High-Entropy Metal–Inorganic Frameworks

Finally, we extend the kinetic and entropic stabilization concept to other frameworks, such as the inorganic coordination polymers known as Prussian blue analogues (PBA). This class of structures has broad applications in electrocatalysis, rechargeable batteries, and supercapacitors [59]. During the non-equilibrium reaction process, the metal nodes in PBA frameworks, linked to ferrocyanide groups, can be occupied by a variety of metal ions (Figure 4a). Prototypical high-entropy MgMnFeNiCu and MnFeCoNiCu PBAs were produced, with their compositions measured by ICP analysis (Table S18). FTIR spectra confirmed the strong absorption band of the M—C≡N—Fe stretching vibration at 2080 cm^{-1} (Figure S76). TGA analysis confirmed the decomposition temperature of 300∼400°C (Figure S77). XRD patterns revealed single-phase cubic FCC structures with the *Fm*−3*m* space group of MgMnFeNiCu PBA (Figure 4b, Table S19) and MnFeCoNiCu PBA (Figure S78, Table S20). Similar to the above MOF materials, rapid reaction kinetics and increased configurational entropy significantly reduced the crystallinity of PBAs. Therefore, the produced PBAs exhibited a polycrystalline structure composed of numerous PBA nanoparticles, with a calculated grain size of approximately 16 nm based on the XRD (220) peaks, rather than conventional large single-crystalline particles (Figure S79). Mesoporous voids were formed between the nanoparticles (Figure S80). HAADF-STEM EDS maps showed the homogeneous distribution of all the constituent metals, confirming the high degree of configurational disorder (Figure 4c).

Furthermore, the electrochemical behavior of the high-entropy PBAs, as well as the corresponding single-component PBAs, was investigated by cyclic voltammetry (CV) in 1 M Na_2SO_4 at varied scan rates from 5 to 200 mV/s (Figures 4d and S81–S87). At each scan rate, the calculated specific capacitances of high-entropy MgMnFeNiCu PBA and MnFeCoNiCu PBA were higher than those of their single-component PBA counterparts (Figure 4e). This highlights the potential of synergistic interactions among multiple elements within high-entropy frameworks to enhance performance.

3 | Conclusions

This research establishes a versatile methodology to create a diverse range of high-entropy MOFs and inorganic coordination polymers. Rapid reaction kinetics and configurational entropy allow the integration of various otherwise-immiscible metals, including noble metals, into a single-phase MOF framework with atomically uniform dispersion. Meanwhile, kinetics and entropy play key roles in MOF structural parameters such as crystallinity, defect density, pore structure, homogeneity, and electrochemical performance, enabling flexible regulation of their fundamental characteristics. Additionally, incorporating multiple elements into single-phase coordination polymers in nearly arbitrary proportions creates an almost limitless compositional space for new materials. This offers a vast potential for leveraging artificial intelligence (AI) to accelerate the development of novel materials [60]. Meanwhile, the one-step, continuous, and scalable aerosol process adopted here is well-suited for high-throughput production compared to batch operations under near-equilibrium conditions [61], allowing rapid preparation of a large number of samples simply by adjusting the reactant composition (Figure S88). The resulting experimental data could be used to refine and optimize deep learning models. Therefore, the technical route developed here provides a new potential platform for iterative improvement through machine learning and high-throughput synthesis loops that would enable rapid screening and development of multi-element MOFs for target applications.

4 | Experimental Section

The experimental section including **chemicals**, **materials synthesis**, **materials characterizations, density functional theory**, and **electrochemical measurements** is provided in the Supporting Information.

Author Contributions

S.L., M.T.S. and C.C.D. conceived the idea; S.L. designed and synthesized all materials; S.L., M.A.K., S.D., J.L.L., S.G., D.W., Q.K.J, K.W.C., C.S., Z.X.X., Y.L.Z., K.W., and C.C.D. performed the material characterization; C.T.Z., K.H.S., and W.C. performed computational and theoretical analysis; S.L. and J.S.L. performed the electrochemical tests; J.H.G., B.M., G.W., J.J.U., and M.T.S. provided the resources. S.L. wrote the first draft of the manuscript; W.C., K.H.S., J.J.U., M.T.S., and C.C.D. revised the manuscript; J.J.U., M.T.S., and C.C.D. jointly supervised this work.

Acknowledgements

This work at the University at Buffalo (SUNY) was supported by the DOE Buildings Technology Office under Contract number DEEE-0008675, by the DOE National Energy Technology Laboratory under Grant No. DE-FE0032209, and by the U.S. National Science Foundation, Grant No. CBET-1804996. Work at the Molecular Foundry and the Advanced Light Source at Lawrence Berkeley National Laboratory was supported by the Office of Science, Office of Basic Energy Sciences of the U.S. Department of Energy (DOE) under Contract No. DE-AC02-05CH11231. The soft-line XAS experiments were carried out at 8.0.1 beamline of the Advanced Light Source. This research also used resources of the 28-ID-2 (XPD) beamline and 8-ID (ISS) beamline of the National Synchrotron Light Source II, a U.S. Department of Energy (DOE) Office of Science User Facility operated for the DOE Office of Science by Brookhaven National Laboratory

under Contract no. DE-SC0012704. K.S. acknowledges the ACS Petroleum Research Fund under Doctoral New Investigator Grant 68604-DNI6 for partial support for C.T.Z. This research used computational resources provided by the Center for Computational Research at the University at Buffalo.

Conflicts of Interest

The authors declare no conflicts of interest.

Data Availability Statement

The data that supports the findings of this study are available in the supplementary material of this article.

References

1. Y. Yao, Q. Dong, A. Brozena, et al., "High-entropy Nanoparticles: Synthesis-structure-property Relationships and Data-driven Discovery," *Science* 376 (2022): abn3103, https://doi.org/10.1126/science.abn3103.

2. W. L. Hsu, C. W. Tsai, A. C. Yeh, and J. W. Yeh, "Clarifying the Four Core Effects of High-entropy Materials," *Nature Reviews Chemistry* 8 (2024): 471–485, https://doi.org/10.1038/s41570-024-00602-5.

3. S. Schweidler, M. Botros, F. Strauss, et al., "High-entropy Materials for Energy and Electronic Applications," *Nature Reviews Materials* 9 (2024): 266–281, https://doi.org/10.1038/s41578-024-00654-5.

4. H. Furukawa, K. E. Cordova, M. O'Keeffe, and O. M. Yaghi, "The Chemistry and Applications of Metal-organic Frameworks," *Science* 341 (2013): 1230444, https://doi.org/10.1126/science.1230444.

5. S. J. Lee and S. G. Telfer, "Multicomponent Metal-Organic Frameworks," *Angewandte Chemie International Edition* 62 (2023): 202306341, https://doi.org/10.1002/anie.202306341.

6. Z. Qiu, X. Lu, Y. Li, et al., "Dynamic Confinement and High-Entropy Catalytic Synergy Engineering in Hollow Nano-Metal-Organic Frameworks," *Advanced Materials* 37 (2025): 11662, https://doi.org/10.1002/adma.202511662.

7. A. Roy, S. Kumar, A. Guilherme Buzanich, et al., "Synergistic Catalytic Sites in High-Entropy Metal Hydroxide Organic Framework for Oxygen Evolution Reaction," *Advanced Materials* 36 (2024): 2408114, https://doi.org/10.1002/adma.202408114.

8. X. Mu, M. Yu, X. Liu, et al., "High-Entropy Ultrathin Amorphous Metal–Organic Framework-Stabilized Ru(Mo) Dual-Atom Sites for Water Oxidation," *ACS Energy Letters* 9 (2024): 5763–5770, https://doi.org/10.1021/acsenergylett.4c02552.

9. X. Xiao, S. Tao, H. Lian, et al., "Unveiling the Microscopic Origin of Ultrahigh Initial Coulombic Efficiency of High-Entropy Metal–Organic Frameworks for Sodium Storage," *ACS Nano* 18 (2024): 28444–28455, https://doi.org/10.1021/acsnano.4c11401.

10. S. Qi, K. Zhu, T. Xu, et al., "Water-Stable High-Entropy Metal-Organic Framework Nanosheets for Photocatalytic Hydrogen Production," *Advanced Materials* 36 (2024): 2403328, https://doi.org/10.1002/adma.202403328.

11. W. Xu, H. Chen, K. Jie, Z. Yang, T. Li, and S. Dai, "Entropy-Driven Mechanochemical Synthesis of Polymetallic Zeolitic Imidazolate Frameworks for CO 2 Fixation," *Angewandte Chemie International Edition* 58 (2019): 5018–5022, https://doi.org/10.1002/anie.201900787.

12. J. Xing, Y. Liu, G. Mathew, et al., "High-Entropy Metal–Organic Frameworks and Their Derivatives: Advances in Design, Synthesis, and Applications for Catalysis and Energy Storage," *Advanced Science* 12 (2025): 2411175, https://doi.org/10.1002/advs.202411175.

13. M. Tamtaji, M. Kazemeini, and A. Kazemi, "High-throughput DFT Screening of Single-metal and High-entropy MOF-74 for Selective CO2/N2 Separation and H2 Storage," *International Journal of Hydrogen Energy* 171 (2025): 151276, https://doi.org/10.1016/j.ijhydene.2025.151276.

14. R. E. Sikma, D. J. Vogel, R. A. Reyes, M. L. Meyerson, P. G. Kotula, and D. F. S. Gallis, "High-Entropy Metal-Organic Frameworks (HEMOFs): A New Frontier in Materials Design for CO 2 Utilization," *Advanced Materials* 36 (2024): 2407435, https://doi.org/10.1002/adma.202407435.

15. L. Jiao and H.-L. Jiang, "Metal-Organic-Framework-Based Single-Atom Catalysts for Energy Applications," *Chemistry* 5 (2019): 786–804, https://doi.org/10.1016/j.chempr.2018.12.011.

16. Y. S. Wei, M. Zhang, R. Zou, and Q. Xu, "Metal–Organic Framework-Based Catalysts With Single Metal Sites," *Chemical Reviews* 120 (2020): 12089–12174, https://doi.org/10.1021/acs.chemrev.9b00757.

17. H. Xie, N. Liu, Q. Zhang, et al., "A Stable Atmospheric-pressure Plasma for Extreme-temperature Synthesis," *Nature* 623 (2023): 964–971, https://doi.org/10.1038/s41586-023-06694-1.

18. B. Wang, C. Wang, X. Yu, et al., "General Synthesis of High-entropy Alloy and Ceramic Nanoparticles in Nanoseconds," *Nature Synthesis* 1 (2022): 138–146, https://doi.org/10.1038/s44160-021-00004-1.

19. Y. Yao, Z. Huang, P. Xie, et al., "Carbothermal Shock Synthesis of High-entropy-alloy Nanoparticles," *Science* 359 (2018): 1489–1494, https://doi.org/10.1126/science.aan5412.

20. C. Yang, B. H. Ko, S. Hwang, et al., "Overcoming Immiscibility Toward Bimetallic Catalyst Library," *Science Advances* 6 (2020): aaz6844, https://doi.org/10.1126/sciadv.aaz6844.

21. T. Li, Y. Yao, Z. Huang, et al., "Denary Oxide Nanoparticles as Highly Stable Catalysts for Methane Combustion," *Nature Catalysis* 4 (2021): 62–70, https://doi.org/10.1038/s41929-020-00554-1.

22. Y. Yao, Z. Huang, L. A. Hughes, et al., "Extreme Mixing in Nanoscale Transition Metal Alloys," *Matter* 4 (2021): 2340–2353.

23. S. Liu, C. Dun, Q. Jiang, et al., "Challenging Thermodynamics: Combining Immiscible Elements in a Single-phase Nano-ceramic," *Nature Communications* 15 (2024): 1167, https://doi.org/10.1038/s41467-024-45413-w.

24. S. Liu, C. Dun, F. Yang, et al., "A General Flame Aerosol Route to Kinetically Stabilized Metal-organic Frameworks," *Nature Communications* 15 (2024): 9365, https://doi.org/10.1038/s41467-024-53678-4.

25. S. Liu, C. W. Pao, J. L. Chen, et al., "A General Flame Aerosol Route to High-entropy Nanoceramics," *Matter* 7 (2024): 3994–4013.

26. H.-B. Cui, Y. Wang, Y.-C. Wang, C. Chen, G. Guan, and M.-Y. Han, "From Multinary Solid Solutions to High-Entropy Nanomaterials," *ACS Nano* 19 (2025): 40641–40661, https://doi.org/10.1021/acsnano.5c16283.

27. S. Liu, C. Dun, J. J. Urban, and M. T. Swihart, "Non-Equilibrium Synthesis Methods to Create Metastable and High-Entropy Nanomaterials," *Advanced Science* 13 (2026): 21953, https://doi.org/10.1002/advs.202521953.

28. A. Kastengren, J. Ilavsky, J. P. Viera, et al., "Measurements of Droplet Size in Shear-driven Atomization Using Ultra-small Angle X-ray Scattering," *International Journal of Multiphase Flow* 92 (2017): 131–139, https://doi.org/10.1016/j.ijmultiphaseflow.2017.03.005.

29. S. Liu, M. Shah, S. Rao, et al., "Flame Aerosol Synthesis of Hollow Alumina Nanoshells for Application in Thermal Insulation," *Chemical Engineering Journal* 428 (2022): 131273, https://doi.org/10.1016/j.cej.2021.131273.

30. M. Eslamian, M. Ahmed, and N. Ashgriz, "Modeling of Solution Droplet Evaporation and Particle Evolution in Droplet-to-Particle Spray Methods," *Drying Technology* 27 (2009): 3–13, https://doi.org/10.1080/07373930802565665.

31. S. S. Aamlid, M. Oudah, J. Rottler, and A. M. Hallas, "Understanding the Role of Entropy in High Entropy Oxides," *Journal of the American Chemical Society* 145 (2023): 5991–6006, https://doi.org/10.1021/jacs.2c11608.

32. C. Oses, C. Toher, and S. Curtarolo, "High-entropy Ceramics," *Nature Reviews Materials* 5 (2020): 295–309, https://doi.org/10.1038/s41578-019-0170-8.

33. X. Cai, Z. Xie, M. Pang, and J. Lin, "Controllable Synthesis of Highly Uniform Nanosized HKUST-1 Crystals by Liquid–Solid–Solution Method," *Crystal Growth & Design* 19 (2019): 556–561, https://doi.org/10.1021/acs.cgd.8b01695.

34. Q. Liu, H. Cong, and H. Deng, "Deciphering the Spatial Arrangement of Metals and Correlation to Reactivity in Multivariate Metal–Organic Frameworks," *Journal of the American Chemical Society* 138 (2016): 13822–13825, https://doi.org/10.1021/jacs.6b08724.

35. M. Folkjaer, L. F. Lundegaard, H. S. Jeppesen, et al., "Pyrolysis of a Metal-organic Framework Followed by In Situ X-ray Absorption Spectroscopy, Powder Diffraction and Pair Distribution Function Analysis," *Dalton Transactions* 51 (2022): 10740–10750.

36. Y. Yang, I. Roh, S. Louisia, et al., "Operando Resonant Soft X-ray Scattering Studies of Chemical Environment and Interparticle Dynamics of Cu Nanocatalysts forco$_2$Electroreduction," *Journal of the American Chemical Society* 144 (2022): 8927–8931, https://doi.org/10.1021/jacs.2c03662.

37. L. Pan, K. M. Adams, H. E. Hernandez, et al., "Porous Lanthanide-Organic Frameworks: Synthesis, Characterization, and Unprecedented Gas Adsorption Properties," *Journal of the American Chemical Society* 125 (2003): 3062–3067, https://doi.org/10.1021/ja028996w.

38. D.-X. Yang, P.-F. Wang, H.-Y. Liu, Y.-H. Zhang, P.-P. Sun, and F.-N. Shi, "Facile Synthesis of Ternary Transition Metal-organic Framework and Its Stable Lithium Storage Properties," *Journal of Solid State Chemistry* 309 (2022): 122947, https://doi.org/10.1016/j.jssc.2022.122947.

39. L. J. Wang, H. Deng, H. Furukawa, et al., "Synthesis and Characterization of Metal–Organic Framework-74 Containing 2, 4, 6, 8, and 10 Different Metals," *Inorganic Chemistry* 53 (2014): 5881–5883, https://doi.org/10.1021/ic500434a.

40. H. Furukawa, F. Gándara, Y.-B. Zhang, et al., "Water Adsorption in Porous Metal–Organic Frameworks and Related Materials," *Journal of the American Chemical Society* 136 (2014): 4369–4381, https://doi.org/10.1021/ja500330a.

41. R. Monteagudo-Olivan, M. Arruebo, P. López-Ram-de-Viu, V. Sebastian, and J. Coronas, "Reactive Gas Atmospheres as a Tool for the Synthesis of MOFs: The Creation of a Metal Hybrid Fumarate With a Controlled Fe/Al Composition Profile," *Journal of Materials Chemistry A* 6 (2018): 14352–14358, https://doi.org/10.1039/C8TA03557A.

42. L.-M. Yang, P. Ravindran, and M. Tilset, "Solid-state Structure and Calculated Electronic Structure, Formation Energy, Chemical Bonding, and Optical Properties of $Zn_4O(FMA)_3$ and its Heavier Congener $Cd_4O(FMA)_3$," *Inorganic Chemistry* 52 (2013): 4217–4228.

43. F. Yang, W. Li, and B. Tang, "Facile Synthesis of Amorphous UiO-66 (Zr-MOF) for Supercapacitor Application," *Journal of Alloys and Compounds* 733 (2018): 8–14, https://doi.org/10.1016/j.jallcom.2017.10.129.

44. S. J. McCormack and A. Navrotsky, "Thermodynamics of High Entropy Oxides," *Acta Materialia* 202 (2021): 1–21, https://doi.org/10.1016/j.actamat.2020.10.043.

45. T. D. Bennett, J.-C. Tan, Y. Yue, et al., "Hybrid Glasses From Strong and Fragile Metal-organic Framework Liquids," *Nature Communications* 6 (2015): 8079, https://doi.org/10.1038/ncomms9079.

46. H. Xu, Z. Zhang, J. Liu, et al., "Entropy-stabilized Single-atom Pd Catalysts via High-entropy Fluorite Oxide Supports," *Nature Communications* 11 (2020): 3908, https://doi.org/10.1038/s41467-020-17738-9.

47. P. Dong, Y. Wang, A. Zhang, T. Cheng, X. Xi, and J. Zhang, "Platinum Single Atoms Anchored on a Covalent Organic Framework: Boosting Active Sites for Photocatalytic Hydrogen Evolution," *Acs Catalysis* 11 (2021): 13266–13279, https://doi.org/10.1021/acscatal.1c03441.

48. X. Hai, S. Xi, S. Mitchell, et al., "Scalable Two-step Annealing Method for Preparing Ultra-high-density Single-atom Catalyst Libraries," *Nature Nanotechnology* 17 (2022): 174–181, https://doi.org/10.1038/s41565-021-01022-y.

49. L. Han, H. Cheng, W. Liu, et al., "A Single-atom Library for Guided Monometallic and Concentration-complex Multimetallic Designs," *Nature Materials* 21 (2022): 681–688, https://doi.org/10.1038/s41563-022-01252-y.

50. J. Chang, W. Jing, X. Yong, et al., "Synthesis of Ultrahigh-metal-density Single-atom Catalysts via Metal Sulfide-mediated Atomic Trapping," *Nature Synthesis* 3 (2024): 1427–1438, https://doi.org/10.1038/s44160-024-00607-4.

51. C. R. Wang, J. M. Stansberry, R. Mukundan, et al., "Proton Exchange Membrane (PEM) Water Electrolysis: Cell-level Considerations for Gigawatt-scale Deployment," *Chemical Reviews* 125 (2025): 1257–1302, https://doi.org/10.1021/acs.chemrev.3c00904.

52. J. Liang, J. Zheng, D. Wierzbicki, et al., "Rhenium-Doping to Promote Structural Evolution of Metallic Iridium to Oxides on Platinum Nanowire Bundles for Acidic Oxygen Evolution," *Angewandte Chemie* 137 (2025): 202512317, https://doi.org/10.1002/ange.202512317.

53. H. Zeng, Z. Chen, Q. Jiang, et al., "Sustainable and Cost-efficient Hydrogen Production Using Platinum Clusters at Minimal Loading," *Nature Communications* 16 (2025): 4314, https://doi.org/10.1038/s41467-025-59450-6.

54. S. Dasari, A. Sharma, C. Jiang, et al., "Exceptional Enhancement of Mechanical Properties in High-entropy Alloys via Thermodynamically Guided Local Chemical Ordering," *Proceedings of the National Academy of Sciences* 120 (2023): 2211787120, https://doi.org/10.1073/pnas.2211787120.

55. Z. Huang, T. Li, B. Li, et al., "Tailoring Local Chemical Ordering via Elemental Tuning in High-entropy Alloys," *Journal of the American Chemical Society* 146 (2024): 2167–2173, https://doi.org/10.1021/jacs.3c12048.

56. T. Li, T. Liu, S. Zhao, et al., "Ultra-strong Tungsten Refractory High-entropy Alloy via Stepwise Controllable Coherent Nanoprecipitations," *Nature Communications* 14 (2023): 3006, https://doi.org/10.1038/s41467-023-38531-4.

57. P.-Y. Liu, B. Zhang, R. Niu, et al., "Engineering Metal-carbide Hydrogen Traps in Steels," *Nature Communications* 15 (2024): 724, https://doi.org/10.1038/s41467-024-45017-4.

58. T. Wei, J. Zou, X. Zhou, et al., "High-entropy Assisted Capacitive Energy Storage in Relaxor Ferroelectrics by Chemical Short-range Order," *Nature Communications* 16 (2025): 807, https://doi.org/10.1038/s41467-025-56181-6.

59. A. Simonov, T. De Baerdemaeker, H. L. B. Boström, et al., "Hidden Diversity of Vacancy Networks in Prussian Blue Analogues," *Nature* 578 (2020): 256–260, https://doi.org/10.1038/s41586-020-1980-y.

60. A. Merchant, S. Batzner, S. S. Schoenholz, M. Aykol, G. Cheon, and E. D. Cubuk, "Scaling Deep Learning for Materials Discovery," *Nature* 624 (2023): 80–85, https://doi.org/10.1038/s41586-023-06735-9.

61. N. J. Szymanski, B. Rendy, Y. Fei, et al., "An Autonomous Laboratory for the Accelerated Synthesis of Inorganic Materials," *Nature* 624 (2023): 86–91, https://doi.org/10.1038/s41586-023-06734-w.

Supporting Information

Additional supporting information can be found online in the Supporting Information section.

Supporting File 1: adma74201-sup-0001-SuppMat.pdf.

Supporting File 2: adma74200-sup-0002-VideoS1.mp4.

Supporting File 3: adma74201-sup-0003-VideoS2.mp4.